

2020-01-08

Hybrid plasmonic photoreactors as visible light-mediated bactericides

Xingda An, Nathchar Naowarajna, Pinghua Liu, Björn M Reinhard. 2020. "Hybrid Plasmonic Photoreactors as Visible Light-Mediated Bactericides.." ACS Appl Mater Interfaces, Volume 12, Issue 1, pp. 106 - 116. <https://doi.org/10.1021/acsami.9b14834>

<https://hdl.handle.net/2144/40614>

"Downloaded from OpenBU. Boston University's institutional repository."

Hybrid Plasmonic Photoreactors as Visible Light-Mediated Bactericides

Xingda An^{1, 2}, Nathchar Naowarajna¹, Pinghua Liu¹, and Björn M. Reinhard^{1, 2*}

¹Department of Chemistry, Boston University, Boston, Massachusetts, United States. 02215.

²Photonics Center, Boston University, Boston, Massachusetts, United States. 02215.

Correspondence to: bmr@bu.edu

Abstract

Photocatalytic compounds and complexes, such as tris(bipyridine)ruthenium(II), [Ru(bpy)₃]²⁺, have shown promise as light-mediated bactericides. However, transition metal-based complexes require relatively high concentrations (ppm level) to achieve reliable antibacterial effects. There is consequently a need for new approaches that provide improved efficacy and control of the antibacterial function of these complexes. In this work, we demonstrate strong, visible light-dependent bacterial inactivation with a nanocomposite design that incorporates [Ru(bpy)₃]²⁺ as photocatalyst and a Ag nanoparticle (NP) core as light-concentrating nanoantenna into a plasmonic hybrid photoreactor. The hybrid photoreactor platform is facilitated by a self-assembled lipid membrane that encapsulates the Ag NP and binds the photocatalyst. The lipid membrane renders the nanocomposite biocompatible in the absence of

resonant illumination. Upon illumination, the plasmon-enhanced photoexcitation of the metal-to-ligand-charge-transfer band of $[\text{Ru}(\text{bpy})_3]^{2+}$ prepares the reactive excited state of the complex that oxidizes the nanocomposite membrane and increases its permeability. The photooxidation induces the release of $[\text{Ru}(\text{bpy})_3]^{2+}$, Ag^+ , and peroxidized lipids into the ambient medium, where they interact synergistically to inactivate bacteria. We measured seven orders of magnitude decrease in Gram-positive *Arthrobacter sp.* and four orders of magnitude decrease in Gram-negative *Escherichia coli* (*E. coli*) colony forming units (CFUs) with the photoreactor bactericides after 1-hour of visible light illumination. In both cases the photoreactor exceeds the bactericidal standard of a log reduction value (LRV) of 3, and surpasses the antibacterial effect of free Ag NPs or $[\text{Ru}(\text{bpy})_3]^{2+}$ by more than four orders of magnitude. We also implement the inactivation of a bacterial thin film in a proof-of-concept study.

Key words: photocatalyst, antibiotics, nanoantenna, antibacterial, sterilization, controlled release, biofilm.

Introduction

Effective sterilization and disinfection technologies are essential for human health and well-being, in particular for avoiding microbial infections through contaminated water, food or drugs, or through contact with contaminated surfaces or medical devices and implants. Common antimicrobial strategies, such as autoclaving, UV or gamma irradiation, chemical disinfectants or molecular antibiotics are not applicable to all samples and face various challenges, including high energy consumption, lack of active control mechanisms, collateral damage to biomolecules, and development of microbial resistances. There has been an increasing interest in the development of alternative bacterial inactivation strategies based on both molecular and nanoparticle-based inactivating agents (IAs) in the past decade to address weaknesses and

limitations of conventional strategies. Various molecular and ionic compounds, including metal cations¹, photoreactive complexes²⁻⁴ and selected natural products⁵⁻⁶, have been developed as novel bactericides. Photocatalysts are a particularly interesting group of bactericides, as they are effective against a broad spectrum of bacterial species and as their action can be controlled *via* the irradiation conditions. Tris(bipyridine)ruthenium(II) ($[\text{Ru}(\text{bpy})_3]^{2+}$) and its analogues have been demonstrated to inactivate bacteria by inducing lipid peroxidation and initiating intracellular redox processes.²⁻⁴ Excitation of the metal-to-ligand charge transfer (MLCT) band in $[\text{Ru}(\text{bpy})_3]^{2+}$ at 430 nm creates an excited state that is both a good oxidant and reductant and whose reactivity defines the antibacterial effect of our photocatalyst. However, the MLCT band in $[\text{Ru}(\text{bpy})_3]^{2+}$ has a molar extinction coefficient $< 10,000 \text{ M}^{-1}\text{cm}^{-1}$.⁷ Moderate absorption is one factor that limits the efficacy of the photocatalyst as bactericide and leads to the need of relatively high concentrations (0.1-1 ppm) of the photocatalyst for reliable bacteria inactivation.^{4, 8} Another potential concern is that the ground state reactivity of $[\text{Ru}(\text{bpy})_3]^{2+}$ can initiate undesirable reactions with biomolecules or entire mammalian cells even in the absence of any illumination, and, thus, jeopardize the role of $[\text{Ru}(\text{bpy})_3]^{2+}$ as light-controlled precision bactericide. This is a problem especially for applications of the photocatalyst in solution or tissue where the molecular complex can easily spread through diffusion.

Metal and semiconductor nanoparticles (NPs) have been developed as nanoscale bactericides and can also serve as scaffolds for molecular photocatalysts.⁹⁻¹⁷ Plasmonic nanostructures that support localized surface plasmon resonances (LSPRs), in particular, have been studied for effective bacterial inactivation through photodynamic therapy,^{11, 18} photo-induced reactive oxygen species production^{9-10, 12, 15, 19} or photothermal effect.²⁰ The strong E-field provided by plasmonic NPs can significantly enhance the absorption of molecules localized in their evanescent field.²¹ As the LSPR of Ag NPs at 430 nm overlaps with the MLCT band of $[\text{Ru}(\text{bpy})_3]^{2+}$, localization of the photocatalyst in the evanescent field of the NPs can enhance

[Ru(bpy)₃]²⁺ excited state formation^{7, 22} and potentially improve the performance of [Ru(bpy)₃]²⁺ as bactericide. Furthermore, it is well known that Ag NPs and Ag⁺ ions by themselves also have shown antibacterial effects.^{1, 10, 16-17} Considering the complementarity of the antibacterial properties of Ag NPs and [Ru(bpy)₃]²⁺ photocatalysts, hybrid NPs-[Ru(bpy)₃]²⁺ nanocomposites represent a promising strategy to enhance potency and efficacy of the individual components and to improve the light-mediated control of the antibacterial effect, ideally to switch the NP properties from benign to antibacterial.

In this manuscript, we investigate the light-dependent antibacterial effect of a photoreactor architecture that integrates [Ru(bpy)₃]²⁺ into a lipid-membrane around a Ag NP through systematic *in vitro* studies. We demonstrate that the plasmon-enhanced photooxidation of the passivating lipid membrane around the Ag NP through [Ru(bpy)₃]²⁺ triggers the release of [Ru(bpy)₃]²⁺, Ag⁺, and peroxidized lipids into the ambient medium where the compounds achieve a synergistic antibacterial effect. We quantify the inactivation performance of the photoreactors and the synergistic interactions between the released compounds on planktonic *Arthrobacter sp.* and *E. coli*. Subsequently, we evaluate the antibacterial effect of the photoreactors against colonized bacteria, which are typically more resilient against conventional disinfection techniques than their planktonic counterparts, in a bacteria biofilm model as a proof-of-concept for surface sterilization applications.

Results and Discussions

Characterization of Plasmonic Photoreactors

We illustrate our design of the photoreactor bactericide in **Fig. 1A**. [Ru(bpy)₃]²⁺ is localized around a 45 nm diameter Ag nanoantenna core through a self-assembled lipid layer that ensures both biocompatibility of the hybrid structure, and localization of the photocatalyst in the

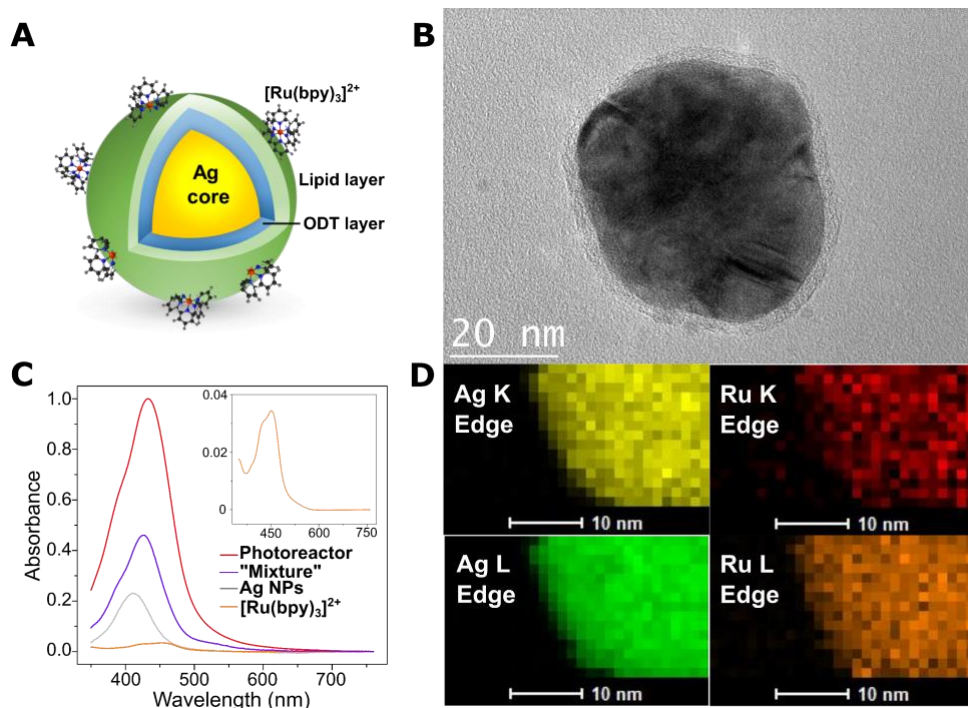


Figure 1. Structural Characterizations of the Photoreactor Nanocomposite.

(A) Scheme of a photoreactor nanocomposite.

(B) HRTEM image of a photoreactor nanocomposite.

(C) UV-vis absorbance spectra of water suspensions of photoreactor nanocomposites (red), Ag NPs (light grey), $[\text{Ru}(\text{bpy})_3]^{2+}$ solution (orange, inset) and a "Mixture" control of Ag NPs colloid and $[\text{Ru}(\text{bpy})_3]^{2+}$ solution (purple).

(D) EDX element maps under STEM mode for Ag and Ru K and L edges in the area indicated in Fig. S1B.

enhanced E-field of the plasmonic nanoantenna when irradiated. We chose Ag NPs as nanoantennas as their LSPR overlaps with the MLCT band of $[\text{Ru}(\text{bpy})_3]^{2+}$ in the range between 415-450 nm. The spectral overlap enables a substantial resonant plasmonic enhancement of the MLCT and photoreactivity of $[\text{Ru}(\text{bpy})_3]^{2+}$, as has been previously demonstrated.^{7, 22} The composition of the lipid layer was inspired by biological membranes with a high degree of unsaturated membrane component that can undergo peroxidation to initiate a photo-controlled release of Ag^+ and $[\text{Ru}(\text{bpy})_3]^{2+}$ (*vide infra*). Specifically, the membrane contained 47 mol % zwitterionic DPPC (1,2-dipalmitoyl-sn-glycero-3-phosphocholine) as skeletal component, 4.5 mol % negatively-charged lipid DOPS (1,2-dioleoyl- sn-glycero-3-phospho-L-serine) to provide electrostatic stabilization of the NPs, and 35 mol % cholesterol as "lubricant" to provide

membrane fluidity. 13.5 mol % Molecular photocatalyst $[\text{Ru}(\text{bpy})_3]^{2+}$ is loaded as “cargo” molecules in the membrane layer.

The lipid layer was tethered to the Ag NPs through an intermediate octadecanethiol (ODT) layer that binds covalently to the metal and sustains hydrophobic interaction with the lipids.²³⁻²⁴ Molecular dynamics simulations in previous studies have indicated that the ODT and lipid layers interdigitate under similar experimental conditions.⁷ To confirm lipid membrane encapsulation of the NP cores, we added a small amount of membrane dye into the lipid layer and mapped the membrane and NP signal, respectively, through correlated fluorescent and darkfield imaging (**Fig. S1C**). The optical colocalization of membrane and NP core signals confirmed successful lipid assembly around the Ag NPs in the photoreactor nanocomposites. High-Resolution TEM (HRTEM) images of the photoreactor nanocomposites further confirm a uniform self-assembled lipid membrane within 10 nm from the Ag surfaces (**Fig. 1B**). The $[\text{Ru}(\text{bpy})_3]^{2+}$ complex acts as membrane stain due to its high electron density and increases the electron contrast of the membrane in the TEM images.²⁵ Statistical analysis of 30 randomly-chosen NPs reveals an average membrane width of 5.7 ± 1.3 nm. Element mapping results generated by Energy Dispersive X-ray Spectroscopy (EDX) in scanning TEM (STEM) mode provide evidence of the spatial colocalization of $[\text{Ru}(\text{bpy})_3]^{2+}$ and Ag NPs in the photoreactor nanocomposite (**Fig. 1D**), further corroborating the successful encapsulation of the Ag NP cores in a self-assembled membrane. The preferential localization of $[\text{Ru}(\text{bpy})_3]^{2+}$ in direct vicinity of the metal NPs is ideal to achieve an E-field-enhanced photoexcitation of $[\text{Ru}(\text{bpy})_3]^{2+}$, as the plasmonic E-field intensity decays rapidly with the increase in separation between metal surface and the photocatalyst. The size of the NPs chosen for this work (diameter ~ 45 nm) combines relatively low radiative losses and moderate dissipative losses, and is therefore ideal for providing high local E-field intensities.²⁶⁻²⁸

We quantified the element compositions of the photoreactor nanocomposite with Inductively Coupled Plasma-Mass Spectrometry (ICP-MS). An average ^{107}Ag concentration of 3834.86 ± 262.00 ppb and a ^{101}Ru concentration of 527.85 ± 3.84 ppb was measured from 0.5 ml of photoreactor suspension. The same concentrations are used for the structural, compositional and bactericidal characterizations unless otherwise noted. UV-Vis spectra confirm substantial enhancement of the absorbance for the MLCT band in the photoreactors (red) when compared with an aqueous solution of $[\text{Ru}(\text{bpy})_3]^{2+}$ (orange, inset) with identical ^{101}Ru concentration (**Fig. 1C**). An enhancement of the MLCT absorbance (at wavelength corresponding to maximum) by a factor of 27 is obtained after correcting for the Ag NP contribution to the absorbance of the photoreactors. The control of a simple mix of Ag NP colloid and $[\text{Ru}(\text{bpy})_3]^{2+}$ solution (“mixture”, purple) at identical ^{107}Ag and ^{101}Ru concentrations as in the photoreactors achieved only a weak enhancement of the MLCT absorbance. This finding provides additional evidence that the spatial colocalization of $[\text{Ru}(\text{bpy})_3]^{2+}$ and Ag NP nanoantennas is required for a substantial plasmonic enhancement.

Characterization of Visible Light-Induced Ag^+ and $[\text{Ru}(\text{bpy})_3]^{2+}$ Release from Photoreactor Nanocomposites

We discovered that the E-field enhanced photocatalytic properties of the photoreactors provide a rational strategy to trigger the release of Ag^+ and $[\text{Ru}(\text{bpy})_3]^{2+}$ through a visible light-initiated and $[\text{Ru}(\text{bpy})_3]^{2+}$ catalyzed oxidation of the photoreactor lipid membrane. We first quantified the release of Ag^+ (**Fig. 2A, B**) and $[\text{Ru}(\text{bpy})_3]^{2+}$ (**Fig. 2C**) from the photoreactors when illuminated with 430 nm LED light or in the dark as a function of time through ICP-MS measurement of ^{107}Ag and ^{101}Ru in the supernatant after removal of the nanocomposites through centrifugation. Unless otherwise noted, we used a 430 nm LED with a power density of 9.76 mW/cm^2 in the sample plane for all bacteria inactivation assays in this work. We observed almost no Ag^+ release from photoreactors in the absence of LED photoactivation (black). However, when

illuminated, the plasmonic photoreactors (“Photoreactor Light”, red) exhibited a much faster Ag⁺ release than the lipid-wrapped Ag NPs with no [Ru(bpy)₃]²⁺ (“LipoAg Light”, blue) (**Fig. 2A**). The release of [Ru(bpy)₃]²⁺ shows overall similar trends as observed for Ag⁺ (**Fig. 2C**). After 1-hour

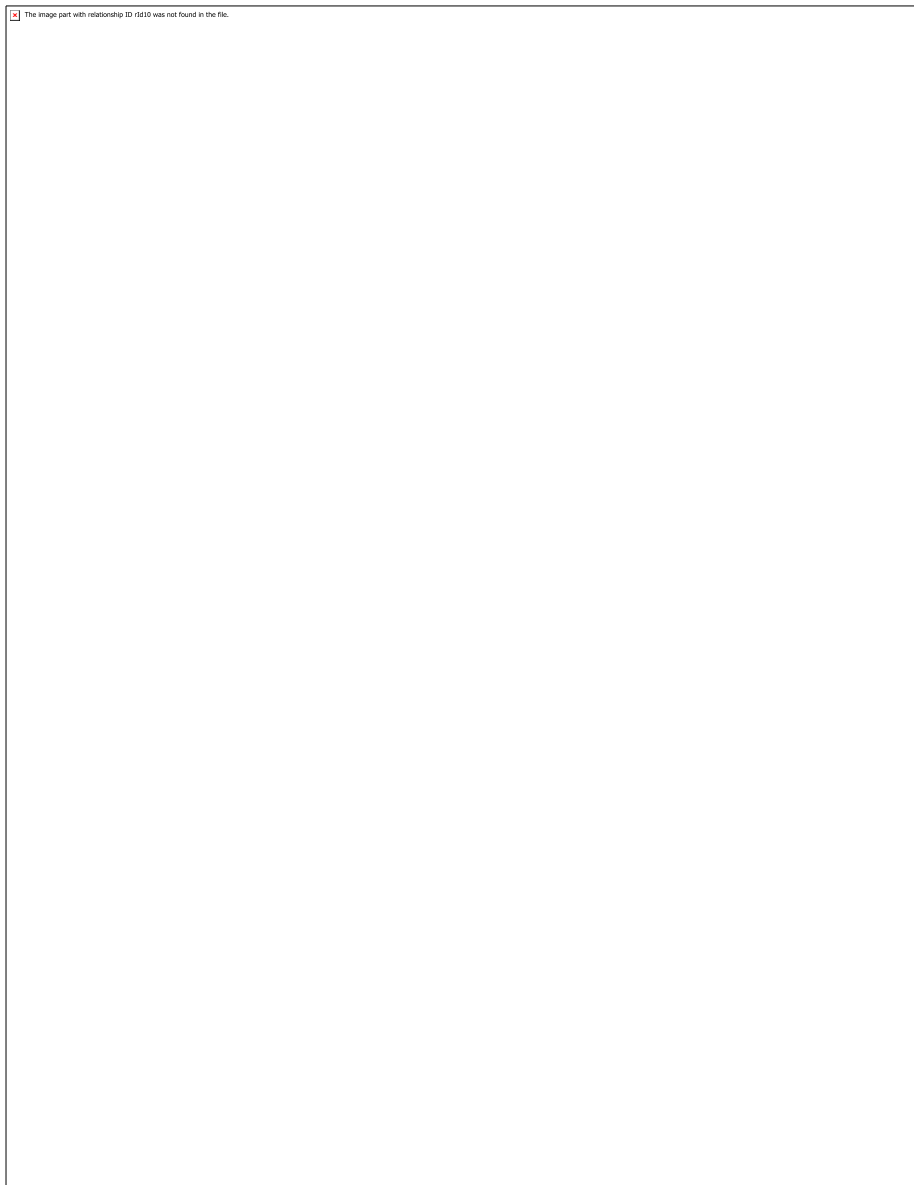


Figure 2. Characterization of Light-mediated Compositional Change in the Photoreactor Nanocomposite.

(A-C) ICP-MS results of Ag⁺ release measured by ¹⁰⁷Ag concentration (A, B) and [Ru(bpy)₃]²⁺ release measured by ¹⁰¹Ru concentration (C) over time. “Mixture Light”: simple mixture control of unwrapped Ag NPs and [Ru(bpy)₃]²⁺ with light; “High ¹⁰¹Ru Light”: photoreactor control with 857 ppb ¹⁰¹Ru with light; “LipoAg Light”: lipid wrapped Ag NPs without [Ru(bpy)₃]²⁺ with light; “Low Cholesterol Light”: photoreactor control with 20 mol % cholesterol with light.

(D-F) TEM images of the photoreactor bacteriocides before illumination (D), with 1 hour of illumination (E) and with 3 hours of illumination (F). Scale bars = 10 nm.

illumination, 237 ppb ¹⁰⁷Ag and 44 ppb ¹⁰¹Ru were released from the photoreactor nanocomposite into the solution, representing 6.2% and 8.3%, respectively, of the total ¹⁰⁷Ag and ¹⁰¹Ru concentration.

Importantly, the concentration of photocatalyst loaded in the membrane provides control over the release of cations from the membrane. This is illustrated by the faster Ag⁺ and [Ru(bpy)₃]²⁺ release by photoreactors containing a higher loading (¹⁰¹Ru concentration: 857 ppb) of [Ru(bpy)₃]²⁺ (“High ¹⁰¹Ru light”, dashed red, **Fig. 2B, C**) than regular photoreactors (¹⁰¹Ru concentration: 528 ppb). Another important observation was that the rate of cation release from the photoreactors is dependent on the composition of the lipid membrane, in particular, on the cholesterol composition. We observed an overall slower ion release rate from a membrane-wrapped nanocomposite control with less cholesterol (20 mol %, “Low Cholesterol Light”) than for normal photoreactors (35 mol % cholesterol) (**Fig. 2B, C**, pink). The concentration of the unsaturated cholesterol in the photoreactor membrane has a significant effect on the light-mediated release kinetics.

We hypothesize that the release of cations from the photoreactors is induced by morphological changes to the photoreactor membrane layer through [Ru(bpy)₃]²⁺-induced photoexcitation. We monitored the membrane around photoreactors with TEM after different photoactivation times with the 430 nm LED. Before illumination, a uniform lipid membrane layer is observed for the photoreactor, as expected (**Fig. 2D**). After 1 hour of illumination, the density of the membrane layer around the NPs decreased (less contrast) while – intriguingly – its width increased, indicating a less densely-packed membrane layer (**Fig. 2E**). A statistical analysis of 20 randomly-chosen particles revealed an average membrane width of 7.7 ± 2.5 nm after illumination, which compares to 5.7 ± 1.3 nm before. After 3 hours, the membrane layer further decreased in density and was barely visible (**Fig. 2F**). In comparison, a lipid-wrapped Ag NP control without [Ru(bpy)₃]²⁺ showed an intact membrane even after 3-hour illumination with 430 nm LED (**Fig. S2C**). We attribute this photo-induced change to the density and morphology of the photoreactor lipid membrane to a continuous lipid peroxidation of the membrane layer. It has

been previously demonstrated that the peroxidation of unsaturated phospholipids (eg., DOPS) by Reactive Oxygen Species and/or photosensitizers can result in the generation of negatively-charged carboxylates, lipid hydroperoxides such as 6-OOH-cholesterol, PS-OOH; and truncated lipid aldehydes.^{29-33 r.} The migration of lipid oxidation products to the membrane/water interface can lead to increase in membrane surface area and potentially the observed increase in membrane thickness.³⁴ Therefore, the photo-driven lipid peroxidation in the photoreactor lipid membrane could initiate the reorganization of the membrane from a dense, closely packed state into a disordered, expanded state with lower density.

The deterioration in the membrane structural integrity is also expected to increase the ion permeability of the photoreactor nanocomposites and lead to ion leakage across the partially photooxidized membrane architecture.^{33, 35} These changes could favor the release of Ag⁺ cations and [Ru(bpy)₃]²⁺ from the photoreactor into the ambient aqueous medium. Ag NPs have been shown to undergo spontaneous oxidative dissolution to release Ag⁺ up to μM concentrations within hours in neutral aqueous solutions facilitated by interactions with O₂ and protons.³⁶⁻³⁷ Furthermore, as the photoexcited state of [Ru(bpy)₃]²⁺ is a strong oxidizer, it participates in the oxidative dissolution of the Ag NP core.³⁶ We measured the oxidative dissolution reaction kinetics of Ag with [Ru(bpy)₃]²⁺. Fits to the concentration *versus* time reveal a nominal reaction order of $n = 0.87$. The first-order ($n = 1$) rate constant was 0.0083 min⁻¹.

We conclude that the photoreactor nanocomposites act essentially as Ag⁺ and [Ru(bpy)₃]²⁺ reservoirs until illumination induces the change in the membrane morphology, triggering a substantial release of Ag⁺ (237 ppb) and [Ru(bpy)₃]²⁺ (44 ppb) into the solution. The visible light induced morphological transformation of the membrane provides a reliable control mechanism for regulating Ag⁺ and [Ru(bpy)₃]²⁺ release both spatially and temporally through an external signal.

***Arthrobacter sp. and E. coli* Inactivation with Photoreactor Bactericides**

The visible light-mediated release of bactericidal Ag⁺ and [Ru(bpy)₃]²⁺ photocatalyst from the photoreactors provides a promising strategy to turn the bactericidal effect on or off. To quantify the efficacy of the photoreactor bactericides for bacterial inactivation, we used *Arthrobacter sp.*, a Gram-positive soil bacteria, as a first test species. *Arthrobacter sp.* has been shown to biodegrade bactericidal pyridine and picolines, and chemically reduce high valence metal cations³⁸⁻⁴¹ and, therefore, presents a robust test case for molecular and metal-based bactericides. We monitored the antibacterial effect of the photoreactor bactericides and

appropriate control groups either in dark or with a focused 430 nm LED with a light power density of 9.76 mW/cm² on the sample, which is significantly lower than the power densities of recent studies that used Near Infrared light or pulsed lasers with powers close to ~1 W/cm².^{18, 20} We used NP: bacteria ratios of 100:1 and calculated the log reduction values (LRVs) of colony-forming units (CFUs) as a function of time as a measure to quantify bacterial inactivation efficacy (see Supplemental Information). An $LRV \geq 3$ (over 3 orders of magnitude reduction in planktonic bacterial CFUs) is considered standard for good bactericidal activity.⁴²⁻⁴³ The

antibacterial effect of the 430 nm LED illumination alone was subtracted from all experimental conditions with illumination to exclude inactivation caused by illumination only. As shown in **Fig. 3A**, the photoreactor bactericide without illumination (black) does not achieve any measurable inactivation. Instead, bacterial growth over the duration of the experiment (1 hour) leads to a negative “LRV”. This result confirms the high biocompatibility of the non-illuminated photoreactor bactericides that arises from their hierarchical architecture with a lipid membrane defining the surface. Importantly, when illuminated, the photoreactor bactericides (red)

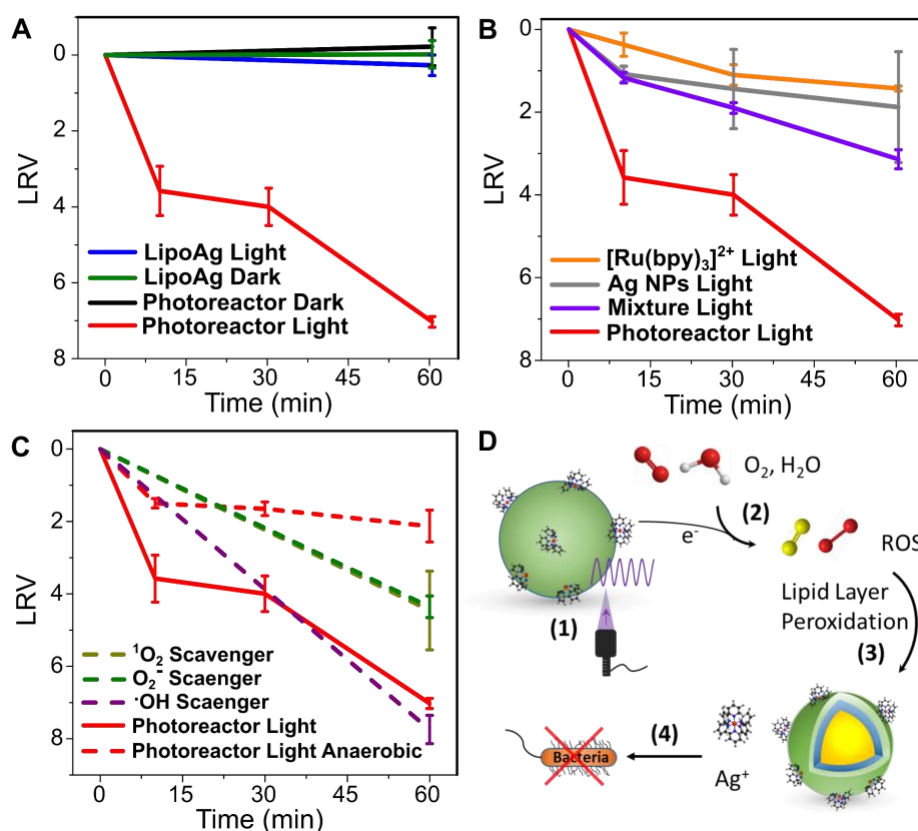


Figure 3. Study of the Inactivation Property and Mechanism of the Photoreactor Bactericides.

(A) Inactivation curves for *Arthrobacter sp.* with photoreactor bactericides and LipoAg control with or without 430 nm LED photoactivation.

(B) Inactivation curves for *Arthrobacter sp.* with just Ag NPs, just [Ru(bpy)₃]²⁺, a Mixture control of Ag NPs and [Ru(bpy)₃]²⁺ solution, and photoreactor with light.

(C) Inactivation curves for *Arthrobacter sp.* with photoreactor bactericides in anaerobic conditions or with singlet oxygen (¹O₂), superoxide (O₂⁻) and hydroxyl radical (·OH) scavengers.

(D) Scheme for the light controlled cation release and inactivation pathway of the photoreactor bactericides.

demonstrate a drastic reduction in *Arthrobacter sp.* CFUs. An LRV of 7.03 (±0.14) is determined for this group after photoactivation for 1 hour. In comparison, membrane-wrapped Ag NPs without [Ru(bpy)₃]²⁺ (“LipoAg”, with/without light: blue/green) did not show any significant bacterial inactivation. These observations prove that the molecular photocatalyst [Ru(bpy)₃]²⁺ is an essential component for the initiation of any significant antibacterial effect. The absence of significant bacterial inactivation for “LipoAg” also excludes a photothermal effect or optically induced hot carrier redox chemistry as causes for the observed inactivation.

We also quantified light-mediated inactivation of Gram-negative bacteria *Escherichia coli* (*E. coli*) (**Fig. S2A**) through photoreactor bactericide and control groups. We observed LRV = 3.93 (\pm 0.66) after 1 hour of photoactivation at 430 nm with the photoreactor bactericides. The lower LRV compared to *Arthrobacter sp.* can be partly because of the presence of an extra outer membrane layer in *E. coli*, which is absent in Gram-positive strains.⁴⁴ For both bacteria, we achieved LRV > 3, and the observation of substantial LRVs for both Gram-positive and negative bacteria confirms that the photoreactor bactericides are broad-spectrum antimicrobial agents.

Quantifying the Synergistic Anti-Bacterial Effect Provided by the Hierarchical Photoreactor Design

To understand the role of the individual components of the photoreactor nanocomposite in the observed bacterial inactivation, we first measured the log reduction obtained with *Arthrobacter sp.* CFUs from each of the individual components. We quantified the antibacterial effect of “free” Ag⁺ or [Ru(bpy)₃]²⁺ solutions of the same concentration as released by the photoreactor under identical visible light illumination as discussed earlier. We also considered unwrapped Ag NPs with identical particle concentration as for the photoreactor, and a “mixture” control of Ag NP colloid and [Ru(bpy)₃]²⁺ solution. As shown in **Fig. 3B** and **Fig. S3A**, both Ag NPs and Ag⁺ alone (with or without illumination) have only a moderate inactivation effect on *Arthrobacter sp.* with LRVs < 2, likely due to the reducing power and metal-resistance of *Arthrobacter sp.*^{39-40, 45} Free [Ru(bpy)₃]²⁺ complex (**Fig. 3B**, orange) achieves LRVs of 1.43 (\pm 0.06) after 1 hour photoactivation and of 0.66 (\pm 0.23) in the dark, which confirms the toxicity of the complex due to ground state reactivity. The simple “mixture” control (**Fig. 3B**, purple), which lacks the preferential localization of [Ru(bpy)₃]²⁺ within the evanescent E-field of the Ag NPs, achieves an LRV of 3.14 (\pm 0.23), which indicates an almost 4-orders-of-magnitude weaker anti-bacterial effect than for the photoreactor bactericides (LRV = 7.03) that contain [Ru(bpy)₃]²⁺ embedded

within the evanescent field of the NPs. This dramatic difference emphasizes the crucial importance of the hierarchical nanoreactor structure for maximizing antibacterial efficacy.

For completeness, we also assessed the inactivation properties of the peroxidized lipid products that are released from the photoreactors. To that end, we separated the lipid components from the photoreactor bactericide after 1 hour of photoactivation and determined the LRVs for *Arthrobacter sp.* (**Fig. S3B**). We obtained LRVs of 2.19 (± 0.38) / 2.39 (± 0.22) without / with 430 nm LED photoexcitation during the inactivation. The essentially identical bactericidal performance rules out a light-driven effect in the peroxidized lipid products, but indicates a chemical effect. We further validated the antibacterial effect of the peroxidized lipids by adding a reducing agent to the isolated lipids prior to their incubation with the bacteria, so as to get rid of the peroxidized lipid products. This treatment reduced the bacteria inactivation of the peroxidation products by one order of magnitude. We measured LRV=1.23 (± 0.20) for the reduced lipid products after illumination for 1 hour (**Fig. S3B**, dotted line) with *Arthrobacter sp.*, which confirms that the peroxidized lipid species contribute to the net antibacterial effect.

Importantly, the LRV of the photoreactor (7.03) significantly exceeds the sum of individual components of Ag NPs, [Ru(bpy)₃]²⁺ and peroxidized lipid components (5.53). As a measure of the gain in antibacterial efficacy resulting from synergistic interactions between the individual components incorporated into the photoreactor, we plotted the time for individual components and the photoreactor to reach LRV=1 (one order of magnitude reduction in bacterial CFUs) for *Arthrobacter sp.* under illumination in a 3-D isobologram (**Fig. S4**). The photoreactors reach LRV = 1 much faster than predicted by the isobole plane, which indicates a strong synergistic amplification of the antibacterial effects of the individual components when combined into the photoreactor. In comparison, the simple mixture control of Ag NPs and [Ru(bpy)₃]²⁺ solution appears close to and above the isobole plane, consistent with a simple additive effect without any obvious synergistic gain.

Elucidating the Mechanism of Bacteria Inactivation through Photoreactor Bactericides

To further characterize the light-controlled Ag^+ and $[\text{Ru}(\text{bpy})_3]^{2+}$ release pathway and associated inactivation mechanism(s), we next performed bacteria inactivation experiments with photoreactors under anaerobic conditions (**Fig. 3C**, red dashed) to probe the effect of oxygen. The photoreactor-associated LRV for *Arthrobacter sp.* with 1-hour illumination dropped to $\text{LRV} = 2.13 (\pm 0.44)$ under anaerobic conditions. This is a clear indicator that O_2 is a key factor in the activation of the antibacterial properties of the photoreactors. Without light, a similar LRV ($= 2.21 \pm 0.19$) is achieved under anaerobic conditions (**Fig. S3A**), indicating that this level of inactivation could be due to light-independent ground state reactivity of the photocatalyst, and/or formation of reactive oxygen species (ROS) produced from H_2O through photoinduced water splitting reactions.

We hypothesized that the photoexcitation of $[\text{Ru}(\text{bpy})_3]^{2+}$ in the presence of O_2 generates ROS to induce the lipid membrane oxidation in the photoreactors, which then subsequently initiates release of antibacterial Ag^+ and $[\text{Ru}(\text{bpy})_3]^{2+}$ into the medium. Three types of ROS are likely to be generated from $[\text{Ru}(\text{bpy})_3]^{2+}$ in H_2O in the presence of O_2 : singlet oxygen ($^1\text{O}_2$), superoxide anion (O_2^-) and/or hydroxyl radicals ($\cdot\text{OH}$).⁴⁶⁻⁴⁸ To test our hypothesis and to determine the specific types of ROS that participate in the inactivation of bacteria, we quantified LRVs for illuminated photoreactors in the presence of different ROS scavengers: sodium azide (scavenger for $^1\text{O}_2$), MnTBAP (scavenger for O_2^-) and mannitol (scavenger for $\cdot\text{OH}$) as demonstrated in previous researches.⁴⁹ As shown in **Fig. 3C**, both $^1\text{O}_2$ (dashed brown) and O_2^- (dotted green) scavengers significantly reduce the inactivation of the bactericides. These two groups achieve almost identical LRVs of around 4 after 1 hour of illumination, which suggests a similar role of $^1\text{O}_2$ and O_2^- in inducing lipid membrane peroxidation and cation release. $\cdot\text{OH}$ scavengers (dashed purple) do not obviously affect the antibacterial activities. This can be

attributed to the relatively short lifetime of $\cdot\text{OH}$ (half-life 10^{-9} s) compared to the other two species (half-life 10^{-6} s).⁵⁰

Based on the above analysis, we summarize the model shown in **Fig. 3D** for the light-driven antibacterial pathway of photoreactor bactericides. Upon resonant illumination of the Ag NP plasmon, rapid E-field-enhanced photoexcitation of $[\text{Ru}(\text{bpy})_3]^{2+}$ generates $\text{Ru}^*(\text{II})$ photoexcited states through MLCT, which can react with O_2 or H_2O in the liquid to produce various ROS. These ROS, as well as the photoexcited $\text{Ru}^*(\text{II})$ state, will then affect the chemical composition of the photoreactor lipid membrane through peroxidation of cholesterol and unsaturated phospholipids (DOPS). These reactions result in changes in chemical composition and the restructuring of the photoreactor membrane, which increases the ion permeability of the photoreactor nanocomposites. Eventually, these morphological changes result in the oxidative dissolution of Ag and release of Ag^+ ions, membrane-bound $[\text{Ru}(\text{bpy})_3]^{2+}$ and peroxidized lipid species into the aqueous solution, where they can subsequently achieve superior antibacterial effects. The visible light-controlled pathway exerts good spatial and temporal control and promise good localized effect of the released bactericidal species.

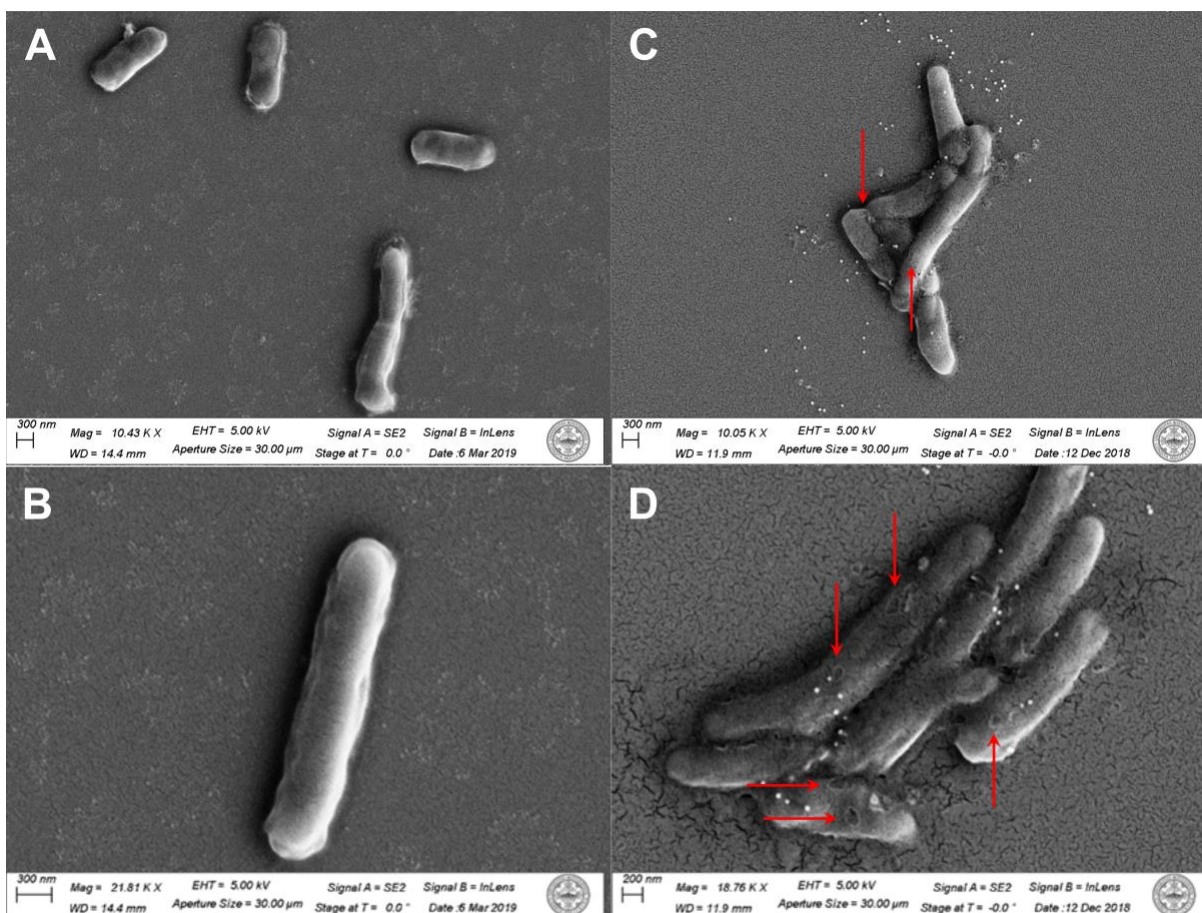


Figure 4. Characterization on the Effect of Photoreactors on Bacteria Surface with SEM.

(A, B) SEM images of the *Arthrobacter* sp. before inactivation

(C, D) SEM images of the *Arthrobacter* sp. after 1 hour of illumination for inactivation with photoreactor bacteriocides. See also **Fig. S5**.

How do the released cations from the photoreactor inactivate the bacteria? We next used Scanning Electron Microscopy (SEM) imaging of *Arthrobacter* sp. before and after inactivation to obtain insights on this question (**Fig. 4, S5**). Notably, after inactivation, a large number of pores with lateral dimensions of tens-to-hundreds of nanometers in diameter are clearly visible in the bacteria cell surface after treatment with our photoreactors (**Fig. 4C, D, S5** circled areas). This perforation effect was unique to the photoreactors, suggesting a cooperative effect by released Ag^+ and $[\text{Ru}(\text{bpy})_3]^{2+}$ as underlying cause. Control experiments using Ag NPs only at an equivalent NPs: bacteria ratio of 100:1 (**Fig. S3C**), an identical concentration of $[\text{Ru}(\text{bpy})_3]^{2+}$ as in the photoreactors (527.85 ppb), or even a 100-fold increased concentration of $[\text{Ru}(\text{bpy})_3]^{2+}$ (**Fig. S3D**) are all insufficient to produce holes in the bacterial cell wall. Only when we

increased the Ag NP concentration by a factor of 100 to achieve a NP: bacteria ratio of 10000:1, did we detected damages of the cell surface (**Fig. S3E, F**). The formation of pores indicate that the effect of the photoreactors are localized on the cell surface, consistent with some earlier Ag-based antibacterial research.¹⁷ We hypothesized that such localized perforation effect could be because (1) of damages to selected bacterial surface ion channels, where structural damage to ion channel proteins could cause the channels to enlarge into pores; and/or (2) the controlled release of the cations adopt a spatial confinement of their effect to just the diffusive vicinity of the photoreactor nanocomposites. Ag⁺ cations have been demonstrated to bind to surface proteins that contains sulfhydryl (-SH) groups,¹ and to induce local membrane damage to ion channels, such as K⁺ channels or Non-Selective Cation Channels (NSCCs).⁵¹ Our EDX measurements confirmed Ag⁺ binding to the bacteria (*Arthrobacter sp.*) under our experimental conditions (**Fig. S6**). Besides, the oxidative properties of [Ru(bpy)₃]²⁺ could accelerate the membrane perforation effect through formation of truncated aldehyde species from unsaturated membrane components and, thus, contribute to the experimentally observed efficient membrane perforation.³³ Such damages to the cell-wall and cell membrane integrity abrogate the osmotic pressure balance across the cell membrane, and would eventually leads to cell death. Furthermore, it is conceivable that these bacterial cell surface pores increase the permeability for bactericidal Ag⁺, [Ru(bpy)₃]²⁺ and peroxidized lipids. The reactive species can cause intracellular damage after passing the protective bacterial membranes, further enhancing bacterial cell death.

Inactivation of a Bacterial Biofilm

The superb inactivation of planktonic bacteria provided by photoreactor bactericides motivates the characterization of their efficacy against bacterial biofilms, where bacteria are embedded in a complex extracellular matrix (ECM) composed of polysaccharides, proteins and nucleic acids secreted by the cells. Due to the protective function of the ECM, bacteria in a biofilm typically

show higher resilience against conventional molecular and nanoscale IAs,⁵²⁻⁵³ motivating the development of new strategies against bacterial biofilms. In this section, we test the efficiency of the photoreactor bactericides against resilient bacterial biofilms.

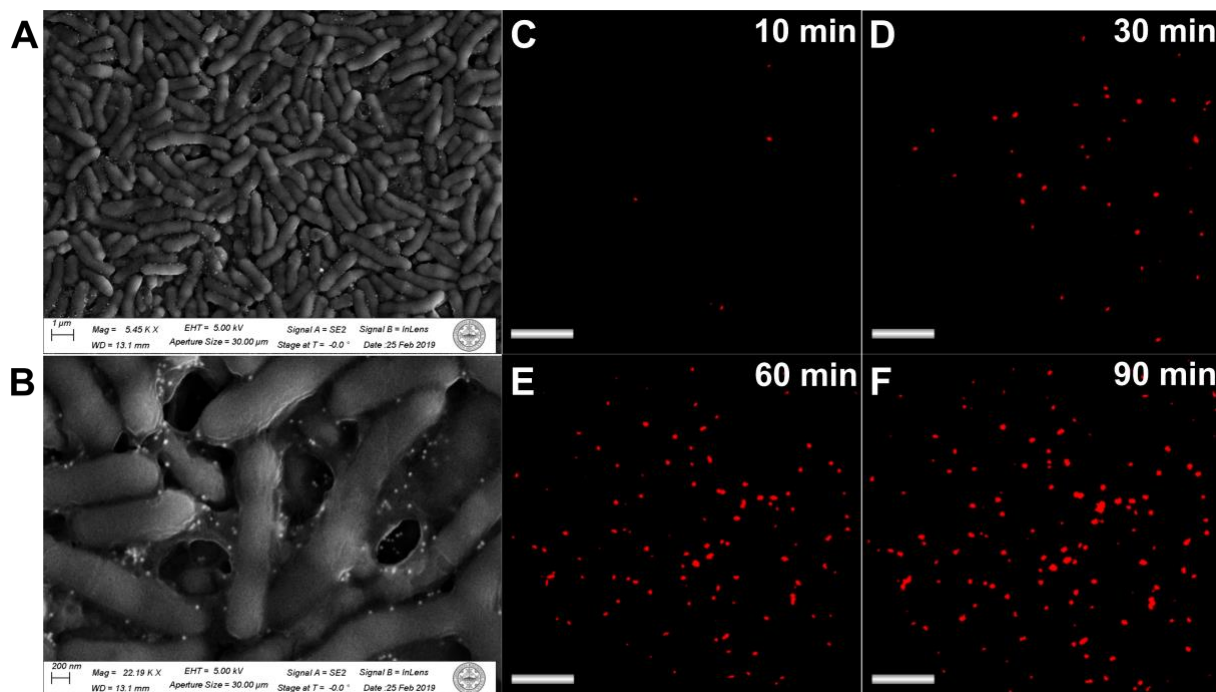


Figure 5. Characterization of the Inactivation of *Arthrobacter sp.* Biofilm.

(A, B) SEM images of the biofilm incubated with photoreactor bactericides (1×10^{10} NPs/mL) for 1h.

(C-F) Fluorescence images of a time course of biofilm inactivation after stained with Propidium Iodide taken at (C) 10 minutes, (D) 30 minutes, (E) 60 minutes and (F) 90 minutes of illumination. Scale bar= $4 \mu\text{m}$.

We cultured *Arthrobacter sp.* into biofilms on silicon wafers and glass slide substrates in Peptone Yeast Extract Glucose (PYEG) media for 7 days in the dark at 37°C using a previously reported protocol.⁵² The biofilm was then incubated with the photoreactor bactericides (1×10^{10} NPs/mL) at room temperature for 1h. **Fig. 5A, B** shows representative Scanning Electron Microscopy (SEM) images of the biofilm after incubation with photoreactors. The images show densely packed bacteria connected by extracellular matrix (ECM). Darkfield Microscope image illustrate a multilayer bacterial film with live bacteria (**Fig. S7**). The photoreactor-treated bacterial biofilm samples were covered by a glass slide and illuminated by white light from a halogen lamp that has a measured power density of 105 mW/cm^2 in the sample plane for up to 90 min. Propidium iodide (PI) staining was used to monitor the illumination time course for

inactivation efficacy as was previously described.⁵⁴ PI is specific to dead or dying cells and is not permeable through intact membranes. After incubation of the photoreactor-containing biofilms with PI, fluorescence images of the biofilm were taken after 10, 30, 60, 90 min of white light illumination (**Fig. 5C-F**). The images show an increase in PI fluorescence intensity in the film as function of time, confirming that the photoreactors are effective against the biofilm. We also performed control experiments of (1.) biofilms exposed to visible light illumination in the absence of photoreactors, and (2.) biofilms with photoreactors but without photoactivation (**Fig. S8**). Neither controls demonstrated noticeable inactivation even after 90 min compared to the photoreactors with photoactivation, confirming that the inactivation effect indeed derives from the photo-induced effect of the photoreactor bactericides.

Conclusion

In summary, we demonstrate visible light-controlled bacteria inactivation from a hybrid photoreactor bactericide architecture incorporating Ag NPs as plasmonic nanoantennas and $[\text{Ru}(\text{bpy})_3]^{2+}$ as photoredox initiator. We have demonstrated that the hierarchical nanostructures are stable and biocompatible in the absence of illumination, when the membrane encapsulating the NPs remains intact. In contrast, low power visible light illumination induces the degradation of the NP membrane, triggers the release of Ag^+ and $[\text{Ru}(\text{bpy})_3]^{2+}$ from the photoreactors, initiates damages to bacterial membranes and cell walls, and ultimately leads to cell death. The released bactericidal species generated by the photoreactor act synergistically to inactivate Gram-positive and negative bacteria in solution and colonized as a biofilm. The hierarchical photoreactor approach significantly enhances the antibacterial efficacy of the photocatalyst as bactericides. The photoreactor composites released lower concentrations of ^{101}Ru (44 ppb) and required lower light power densities ($< 10 \text{ mW/cm}^2$) than previous studies of free $[\text{Ru}(\text{bpy})_3]^{2+}$ that used ppm levels of ^{101}Ru ^{4, 8} and power densities of 1 W/cm^2 to achieve reliable bacteria inactivation.^{18, 20} The photoreactor bactericides achieved over 7 orders of magnitude reduction

for *Arthrobacter sp.* CFUs, and around 4 orders reduction for *E.coli*. The visible light-mediated release pathway also provides additional levels of control for the initiation of inactivation, which paves the path to spatial and temporal regulation of the antibacterial activity. The photoreactor bactericides introduced in this work provide an alternative broad-spectrum antimicrobial strategy with a broad range of applications, ranging from inactivating of bacteria on surfaces and medical devices to wound sterilization.

Materials and Methods

Preparation of the Plasmonic Photoreactor Bactericides

Lipid mixture containing chloroform solutions of 4.5 mol % DOPS, 47 mol % DPPC and 35 mol % cholesterol (all from Avanti Polar Lipids) is mixed with 13.5 mol % methanol solution of “cargo” photocatalyst [Ru(bpy)₃]²⁺ (Sigma Aldrich) to have a total amount of 1.15 μmol. The mixture was rotary evaporated at 34 °C for 10 minutes to form a thin film before being desiccated overnight in a Round Bottom Flask (RBF). Liposomes were generated by tip sonication of the mixture in water suspensions. The liposomes were then combined with 10¹⁰ Ag NPs (hydrodynamic diameter 44.23±0.62 nm measured by Dynamic Light Scattering, DLS) in the presence of octadecanethiol (ODT, Sigma Aldrich). The ODT binds to the Ag NP through covalent interaction and allows tethering of the lipid through hydrophobic interactions. The NPs/lipids/ODT mixture was shaken and incubated at room temperature for 12 hours to yield a uniform yellow suspension. The suspension was then centrifuged, washed with water, combined and stored at 4°C for later use.

Preparation of Bacteria and Inactivation Assays

One colony of *Arthrobacter sp.* (NRRL B3728) was inoculated in ISP2 media and incubated at 28 °C for 16 hours at 180 rpm on a shake incubator. An approximated 10⁹ bac/mL bacterial

suspension in growth media and 10^{11} bactericides/mL water suspension were mixed equivocally. Growth media was added to yield an inactivation mixture containing 10^{10} NPs and 10^8 bacteria (100:1 ratio) in 300 μ L total volume. Inactivation experiments were carried out in glass cuvettes (Starna Cells) with 1 cm light paths; and with illumination of a focused 430 nm LED (ThorLabs). The LED was measured to generate an incident light power of 105 mW over an 18.5 mm diameter light spot, generating an incident power density of 9.76 mW/cm². After the inactivation assays, the mixture was diluted with media and spread and plated on ISP2/LB agar plates to form visible colonies and to be counted for viable colony-forming units (CFUs) at 10 min, 30 min and 1 h of inactivation. We compared the number of CFUs with a Feed group that was kept in dark and had an identical concentration of bacteria and liquid volume but does not contain any inactivating agents. We calculated Log Reduction Values (LRVs) based on experimentally measured colony-forming units (CFUs) obtained for various experimental conditions relative to the Feed. The effect of LED only is accounted for by subtracting the LRVs obtained at different time points with LED only and no photoreactor from LRVs of each with-photoactivation group.

Preparation and Inactivation of Bacterial Biofilms

The preparation of biofilm from *Arthrobacter sp.* was performed following reported procedure.⁵² A colony of *Arthrobacter sp.* was inoculate and incubated at 28 °C for 16 hours at 180 rpm for 16 hours. Then, 50 μ L of this overnight culture was inoculated in a glass test tube containing 5 mL of PYEG media to give a cell concentration of 10^5 bacteria/ml. A piece of either silicon wafer or glass slide (VWR) is put into the test tube as a growth substrate for the biofilms. The cells were cultured at 28 °C under static condition for 7 days prior to the inactivation study. At day 7, photoreactor nanocomposites at a concentration of 10^{10} NPs/mL were added to the growth solution for all groups except the “no photoreactor” control, and incubated at room temperature in dark for 1 hour. For SEM imaging, biofilms on silicon wafer substrate were used, fixed with 4% formaldehyde and imaged. For inactivation of the biofilm, 500 nM of propidium iodide (PI)

solution was first used to stain the bacteria. After incubation at room temperature in dark for 15 minutes, inactivation and fluorescence imaging of biofilms was carried out on an Olympus Inverted Microscope. For inactivation, a tungsten lamp with a 0.0004 mW measured light power was used through a condenser. We measure the light spot generated by the condenser to have a 22 μm diameter, thus giving a power density of 105 mW/cm². The biofilm was imaged after 0, 10 min, 30 min, 60 min and 90 min of illumination.

Associated Content

Supporting Information

Eight supplemental figures and supplemental experimental procedures are included in Supporting Information.

Author Information

Corresponding Author

Björn M. Reinhard: bmr@bu.edu

Author Contributions

B.M.R. and X.A. conceived the study. X.A. and N.N. conducted the experiments. B.M.R. and P.L. supervised the experiments. All authors contributed to and approved of the manuscript.

Funding Sources

This work was in part funded by the National Science Foundation through grant CBET-1822246.

Acknowledgements

The authors thank Dr. Alexey Nikiforov for discussions on TEM imaging and EDX element mapping.

References

1. Morones-Ramirez, J. R.; Winkler, J. A.; Spina, C. S.; Collins, J. J., Silver enhances antibiotic activity against gram-negative bacteria. *Sci Transl Med* **2013**, *5* (190), 190ra81.
2. Lei, W.; Zhou, Q.; Jiang, G.; Zhang, B.; Wang, X., Photodynamic inactivation of Escherichia coli by Ru (II) complexes. *Photochemical & Photobiological Sciences* **2011**, *10* (6), 887-890.
3. Shao, Q.; Xing, B., Enzyme responsive luminescent ruthenium (II) cephalosporin probe for intracellular imaging and photoinactivation of antibiotics resistant bacteria. *Chemical Communications* **2012**, *48* (12), 1739-1741.
4. Arenas, Y.; Monro, S.; Shi, G.; Mandel, A.; McFarland, S.; Lilge, L., Photodynamic inactivation of Staphylococcus aureus and methicillin-resistant Staphylococcus aureus with Ru (II)-based type I/type II photosensitizers. *Photodiagnosis and photodynamic therapy* **2013**, *10* (4), 615-625.
5. Clardy, J.; Fischbach, M. A.; Walsh, C. T., New antibiotics from bacterial natural products. *Nature biotechnology* **2006**, *24* (12), 1541.
6. Saleem, M.; Nazir, M.; Ali, M. S.; Hussain, H.; Lee, Y. S.; Riaz, N.; Jabbar, A., Antimicrobial natural products: an update on future antibiotic drug candidates. *Natural product reports* **2010**, *27* (2), 238-254.
7. An, X.; Stelter, D.; Keyes, T.; Reinhard, B. M., Plasmonic Photocatalysis of Urea Oxidation and Visible-Light Fuel Cells. *Chem* **2019**, *5* (8), 2228-2242.
8. Parakh, P.; Gokulakrishnan, S.; Prakash, H., Visible light water disinfection using [Ru (bpy) 2 (phenanthroline)](PF6) 2· 2H2O and [Ru (phenanthroline) 3] Cl2· 2H2O complexes and their effective adsorption onto activated carbon. *Separation and Purification Technology* **2013**, *109*, 9-17.
9. Booshehri, A. Y.; Chun-Kiat Goh, S.; Hong, J.; Jiang, R.; Xu, R., Effect of depositing silver nanoparticles on BiVO4 in enhancing visible light photocatalytic inactivation of bacteria in water. *J. Mater. Chem. A* **2014**, *2* (17), 6209-6217.
10. Planas, O.; Macia, N.; Agut, M.; Nonell, S.; Heyne, B., Distance-Dependent Plasmon-Enhanced Singlet Oxygen Production and Emission for Bacterial Inactivation. *J Am Chem Soc* **2016**, *138* (8), 2762-8.
11. Khlebtsov, B. N.; Tuchina, E. S.; Khanadeev, V. A.; Panfilova, E. V.; Petrov, P. O.; Tuchin, V. V.; Khlebtsov, N. G., Enhanced photoinactivation of Staphylococcus aureus with nanocomposites containing plasmonic particles and hematoporphyrin. *Journal of Biophotonics* **2013**, *6* (4), 338-351.
12. Zhuang, W.; Yuan, D.; Li, J. R.; Luo, Z.; Zhou, H. C.; Bashir, S.; Liu, J., Highly potent bactericidal activity of porous metal-organic frameworks. *Adv Healthc Mater* **2012**, *1* (2), 225-38.
13. Liu, Y.; Lin, A.; Liu, J.; Chen, X.; Zhu, X.; Gong, Y.; Yuan, G.; Chen, L.; Liu, J., Enzyme-responsive Mesoporous Ruthenium for Combined Chemo-photothermal Therapy of Drug-resistant Bacteria. *ACS applied materials & interfaces* **2019**.
14. Geilich, B. M.; van de Ven, A. L.; Singleton, G. L.; Sepúlveda, L. J.; Sridhar, S.; Webster, T. J., Silver nanoparticle-embedded polymersome nanocarriers for the treatment of antibiotic-resistant infections. *Nanoscale* **2015**, *7* (8), 3511-3519.
15. Macia, N.; Bresoli-Obach, R.; Nonell, S.; Heyne, B., Hybrid Silver Nanocubes for Improved Plasmon-Enhanced Singlet Oxygen Production and Inactivation of Bacteria. *Journal of the American Chemical Society* **2018**, *141* (1), 684-692.
16. Gupta, A.; Mumtaz, S.; Li, C.-H.; Hussain, I.; Rotello, V. M., Combatting antibiotic-resistant bacteria using nanomaterials. *Chemical Society Reviews* **2019**, *48* (2), 415-427.
17. Liu, Y.; Wang, X.; Yang, F.; Yang, X., Excellent antimicrobial properties of mesoporous anatase TiO2 and Ag/TiO2 composite films. *Microporous and Mesoporous Materials* **2008**, *114* (1-3), 431-439.

18. Nazari, M.; Xi, M.; Aronson, M.; Mcrae, O.; Hong, M. K.; Gummuluru, S.; Sgro, A.; Bird, J. C.; Ziegler, L. D.; Gillespie, C., Plasmon-Enhanced Pan-Microbial Pathogen Inactivation in the Cavitation Regime: Selectivity Without Targeting. *ACS Applied Nano Materials* **2019**.
19. Gao, L.; Liu, R.; Gao, F.; Wang, Y.; Jiang, X.; Gao, X., Plasmon-mediated generation of reactive oxygen species from near-infrared light excited gold nanocages for photodynamic therapy in vitro. *ACS nano* **2014**, *8* (7), 7260-7271.
20. Yang, Y.; Deng, Y.; Huang, J.; Fan, X.; Cheng, C.; Nie, C.; Ma, L.; Zhao, W.; Zhao, C., Size - Transformable Metal–Organic Framework–Derived Nanocarbons for Localized Chemo - Photothermal Bacterial Ablation and Wound Disinfection. *Advanced Functional Materials* **2019**, 1900143.
21. Wang, C.; Astruc, D., Nanogold plasmonic photocatalysis for organic synthesis and clean energy conversion. *Chem Soc Rev* **2014**, *43* (20), 7188-216.
22. Mori, K.; Kawashima, M.; Che, M.; Yamashita, H., Enhancement of the Photoinduced Oxidation Activity of a Ruthenium (II) Complex Anchored on Silica - Coated Silver Nanoparticles by Localized Surface Plasmon Resonance. *Angewandte Chemie International Edition* **2010**, *49* (46), 8598-8601.
23. Xu, F.; Reiser, M.; Yu, X.; Gummuluru, S.; Wetzler, L.; Reinhard, B. M., Lipid Mediated Targeting with Membrane-Wrapped Nanoparticles in the Presence of Corona Formation. *ACS Nano* **2015**, *10*, 1189-1200.
24. Yu, X.; Xu, F.; Ramirez, N.-G. P.; Kijewski, S. D.; Akiyama, H.; Gummuluru, S.; Reinhard, B. r. M., Dressing up nanoparticles: A membrane wrap to induce formation of the virological synapse. *ACS nano* **2015**, *9* (4), 4182-4192.
25. Laane, C.; Ford, W. E.; Otvos, J. W.; Calvin, M., Photosensitized electron transport across lipid vesicle walls: enhancement of quantum yield by ionophores and transmembrane potentials. *Proceedings of the National Academy of Sciences* **1981**, *78* (4), 2017-2020.
26. Kelly, K. L.; Coronado, E.; Zhao, L. L.; Schatz, G. C., The optical properties of metal nanoparticles: the influence of size, shape, and dielectric environment. ACS Publications: 2003.
27. Bharadwaj, P.; Novotny, L., Spectral dependence of single molecule fluorescence enhancement. *Optics Express* **2007**, *15* (21), 14266-14274.
28. Ringe, E.; McMahon, J. M.; Sohn, K.; Cobley, C.; Xia, Y.; Huang, J.; Schatz, G. C.; Marks, L. D.; Van Duyne, R. P., Unraveling the effects of size, composition, and substrate on the localized surface plasmon resonance frequencies of gold and silver nanocubes: a systematic single-particle approach. *The Journal of Physical Chemistry C* **2010**, *114* (29), 12511-12516.
29. Yin, H.; Xu, L.; Porter, N. A., Free radical lipid peroxidation: mechanisms and analysis. *Chem Rev* **2011**, *111* (10), 5944-72.
30. Farmer, E. E.; Mueller, M. J., ROS-mediated lipid peroxidation and RES-activated signaling. *Annual review of plant biology* **2013**, *64*, 429-450.
31. Tyurina, Y. Y.; Tyurin, V. A.; Kaynar, A. M.; Kapralova, V. I.; Wasserloos, K.; Li, J.; Mosher, M.; Wright, L.; Wipf, P.; Watkins, S., Oxidative lipidomics of hyperoxic acute lung injury: mass spectrometric characterization of cardiolipin and phosphatidylserine peroxidation. *American Journal of Physiology-Lung Cellular and Molecular Physiology* **2010**, *299* (1), L73-L85.
32. Girotti, A. W., Photosensitized oxidation of membrane lipids: reaction pathways, cytotoxic effects, and cytoprotective mechanisms. *Journal of Photochemistry and Photobiology B: Biology* **2001**, *63* (1-3), 103-113.
33. Bacellar, I. O.; Oliveira, M. C.; Dantas, L. S.; Costa, E. B.; Junqueira, H. C.; Martins, W. K.; Durantini, A. s. M.; Cosa, G.; Di Mascio, P.; Wainwright, M., Photosensitized membrane permeabilization requires contact-dependent reactions between photosensitizer and lipids. *Journal of the American Chemical Society* **2018**, *140* (30), 9606-9615.

34. Weber, G.; Charitat, T.; Baptista, M. S.; Uchoa, A. F.; Pavani, C.; Junqueira, H. C.; Guo, Y.; Baulin, V. A.; Itri, R.; Marques, C. M., Lipid oxidation induces structural changes in biomimetic membranes. *Soft Matter* **2014**, *10* (24), 4241-4247.
35. Ytzhak, S.; Ehrenberg, B., The effect of photodynamic action on leakage of ions through liposomal membranes that contain oxidatively modified lipids. *Photochemistry and photobiology* **2014**, *90* (4), 796-800.
36. Peretyazhko, T. S.; Zhang, Q.; Colvin, V. L., Size-controlled dissolution of silver nanoparticles at neutral and acidic pH conditions: kinetics and size changes. *Environmental science & technology* **2014**, *48* (20), 11954-11961.
37. Roe, D.; Karandikar, B.; Bonn-Savage, N.; Gibbins, B.; Roulet, J.-B., Antimicrobial surface functionalization of plastic catheters by silver nanoparticles. *Journal of antimicrobial chemotherapy* **2008**, *61* (4), 869-876.
38. Jain, R. K.; Dreisbach, J. H.; Spain, J. C., Biodegradation of p-nitrophenol via 1, 2, 4-benzenetriol by an *Arthrobacter* sp. *Appl. Environ. Microbiol.* **1994**, *60* (8), 3030-3032.
39. Margesin, R.; Schinner, F., Heavy metal resistant *Arthrobacter* sp.—A tool for studying conjugational plasmid transfer between Gram - negative and Gram - positive bacteria. *Journal of basic microbiology* **1997**, *37* (3), 217-227.
40. Prasad, K. S.; Ramanathan, A.; Paul, J.; Subramanian, V.; Prasad, R., Biosorption of arsenite (As⁺³) and arsenate (As⁺⁵) from aqueous solution by *Arthrobacter* sp. biomass. *Environmental technology* **2013**, *34* (19), 2701-2708.
41. O'loughlin, E. J.; Sims, G. K.; Traina, S. J., Biodegradation of 2-methyl, 2-ethyl, and 2-hydroxypyridine by an *Arthrobacter* sp. isolated from subsurface sediment. *Biodegradation* **1999**, *10* (2), 93-104.
42. Mascio, C. T.; Alder, J. D.; Silverman, J. A., Bactericidal action of daptomycin against stationary-phase and nondividing *Staphylococcus aureus* cells. *Antimicrobial agents and chemotherapy* **2007**, *51* (12), 4255-4260.
43. Sobotta, L.; Długaszewska, J.; Ziental, D.; Szczolko, W.; Koczorowski, T.; Goslinski, T.; Mielcarek, J., Optical properties of a series of pyrrolyl-substituted porphyrazines and their photoinactivation potential against *Enterococcus faecalis* after incorporation into liposomes. *Journal of Photochemistry and Photobiology A: Chemistry* **2019**, *368*, 104-109.
44. Silhavy, T. J., Classic spotlight: Gram-negative bacteria have two membranes. *Journal of bacteriology* **2016**, *198* (2), 201.
45. Hasan, S. H.; Srivastava, P., Batch and continuous biosorption of Cu²⁺ by immobilized biomass of *Arthrobacter* sp. *Journal of environmental management* **2009**, *90* (11), 3313-3321.
46. Abreu, F. D.; Diógenes, I. C. N.; de França Lopes, L. G.; Sousa, E. H. S.; de Carvalho, I. M. M., Ruthenium (II) bipyridine complexes with pendant anthracenyl and naphthyl moieties: A strategy for a ROS generator with DNA binding selectivity. *Inorganica Chimica Acta* **2016**, *439*, 92-99.
47. Ye, Z.; Song, B.; Yin, Y.; Zhang, R.; Yuan, J., Development of singlet oxygen-responsive phosphorescent ruthenium (II) complexes. *Dalton Transactions* **2013**, *42* (40), 14380-14383.
48. da Silva, R. S.; Marchesi, M. S. P.; Tedesco, A. C.; Mikhailovsky, A.; Ford, P. C., Generation of reactive oxygen species by photolysis of the ruthenium (ii) complex Ru (NH₃)₅ (pyrazine)₂⁺ in oxygenated solution. *Photochemical & Photobiological Sciences* **2007**, *6* (5), 515-518.
49. Nazari, M.; Xi, M.; Lerch, S.; Alizadeh, M. H.; Ettinger, C.; Akiyama, H.; Gillespie, C.; Gummuluru, S.; Erramilli, S.; Reinhard, B. M., Plasmonic Enhancement of Selective Photonic Virus Inactivation. *Sci Rep* **2017**, *7* (1), 11951.

50. Papuc, C.; Goran, G. V.; Predescu, C. N.; Nicorescu, V., Mechanisms of oxidative processes in meat and toxicity induced by postprandial degradation products: A review. *Comprehensive Reviews in Food Science and Food Safety* **2017**, *16* (1), 96-123.
51. Coskun, D.; Britto, D. T.; Jean, Y.-K.; Schulze, L. M.; Becker, A.; Kronzucker, H. J., Silver ions disrupt K⁺ homeostasis and cellular integrity in intact barley (*Hordeum vulgare* L.) roots. *Journal of experimental botany* **2011**, *63* (1), 151-162.
52. Dey, S.; Paul, A., Influence of metal ions on biofilm formation by *Arthrobacter* sp. SUK 1205 and evaluation of their Cr (VI) removal efficacy. *International biodeterioration & biodegradation* **2018**, *132*, 122-131.
53. Galiè, S.; García-Gutiérrez, C.; Miguélez, E. M.; Villar, C. J.; Lombó, F., Biofilms in the food industry: health aspects and control methods. *Frontiers in microbiology* **2018**, *9*, 898.
54. Kim, Y. E.; Chen, J.; Langen, R.; Chan, J. R., Monitoring apoptosis and neuronal degeneration by real-time detection of phosphatidylserine externalization using a polarity-sensitive indicator of viability and apoptosis. *Nature protocols* **2010**, *5* (8), 1396.

Table of Content (TOC) Figure

